# Millimeter-Wave Radar Scheme With Passive Reflector for Uncontrolled Blind Urban Intersection

Dmitrii Solomitckii , Carlos Baquero Barneto , Matias Turunen , Markus Allén , George P. Zhabko, Sergey V. Zavjalov , Sergey V. Volvenko , and Mikko Valkama

*Abstract*—Modern millimeter-wave automotive radars are employed to keep a safe distance between vehicles and reduce the collision risk when driving. Meanwhile, an on-board radar module is supposed to operate in the line-of-sight condition, which limits its sensing capabilities in intersections with obstructed visibility. Therefore, this paper investigates the scheme with passive reflector, enabling the automotive radar to detect an approaching vehicle in the non-line-of-sight (blind) urban intersection. First, extensive radar measurements of the backscattering power are carried out with the in-house assembled millimeter-wave radar equipment. Next, the measured data is employed to calibrate an accurate analytical model, deduced and described in this paper. Finally, the analytical models are deployed to define the optimal parameters of the radar scheme in the particular geometry of the selected intersection scenario. Specifically, it is found that the optimal angular orientation of the reflector is 43.5°, while the 20 m curvature radius shows better performance compared to a flat reflector. Specifically, the curved convex shape increases scattering power by 20 dB in the shadow region and, thus, improves the detection probability of the vehicle, approaching the blind intersection.

*Index Terms*—Automotive radars, collision risk, Kirchhoff approximation, millimeter-wave radar, passive reflector, radar measurement, vehicular systems.

## I. INTRODUCTION

**R**ECENTLY, millimeter-wave (mmWave) automotive radars have started to be actively deployed in both premium as well as lower-budget commercial vehicles [1], in order to improve the safety of pedestrians and drivers. This trend is motivated by new traffic requirements, leading to the reduction of accidents on the road. For example, the European New Car Assessment Programme (NCAP) that started

Dmitrii Solomitckii, Carlos Baquero Barneto, Matias Turunen, Markus Allén, and Mikko Valkama are with the Electrical Engineering Unit, Tampere University, FI-33101 Tampere, Finland (e-mail: dmitrii.solomitckii@tuni.fi; carlos.baquerobarneto@tuni.fi; matias.turunen@tuni.fi; markus.allen@tuni.fi; mikko.valkama@tuni.fi).

George P. Zhabko, Sergey V. Zavjalov, and Sergey V. Volvenko are with the Department of Communication, Peter the Great St. Petersburg Polytechnic University, 195251 Sankt-Peterburg, Russia (e-mail: zhabko_gp@spbstu.ru; zavyalov_sv@spbstu.ru; volk@cee.spbstu.ru).

already in 2016, demands to install at least one Advanced driver-assistance system (ADAS) [2] on the vehicle to receive a five-star safety rating. Among them, Adaptive cruise control, Automatic Emergency Braking, Forward Collision-Avoidance Assist, Intersection Assistant, and Automotive Night Vision are among the most common radar-based ADAS elements deployed in vehicles. Additionally, in the longer term perspective, the automotive radars and other sensing instruments will assist also self-driving or autonomous vehicles [3].

Nevertheless, automotive radars operate in the line-of-sight (LOS) mode, which limits the ability to recognise an approaching vehicle behind a building in an uncontrolled blind urban intersection. As a result, such unawareness about the approaching vehicle leads to the collision risk, even though an ADAS is on-board. This paper extends the research of the radar scheme aided with a passive reflector in [4] and [5], seeking to enable and facilitate detecting a car around the corner. Specifically, in [4], the concept of the radar scheme with passive reflector was originally proposed, including also preliminary measurements. Further, in [5], the variant of the scheme with a raised reflector, mitigating the blockage effect, was suggested. In this paper, we develop and assess the concept further, with notable contributions that can be summarized as follows:

(1) We carry out, report, and analyze an extensive set of radar measurements in a practical and realistic vehicular environment.

(2) We derive an accurate electromagnetic model, building on the measurement data, which can characterize and predict the functionality of the proposed radar scheme.

(3) We use the derived analytical model to define the optimal parameters of the proposed radar scheme for the geometry of the considered environment. Methodology-wise, this can be extended in a straightforward manner to any other practical environment as well.

The rest of the paper is organized as follows. Review of the relevant technologies for the non-line-of-sight (NLOS) radar detection is provided in Section II. Next, Section III explains the measurement equipment and the considered deployment scenario. Section IV introduces the methods for analytical calculations and electromagnetic (EM) modelling. Measurement-based and modeling-based results are described in Sections V and VI, respectively. Finally, conclusions are drawn in Section VII, while an example derivation of the analytical formulas is given in Appendix A.

## II. OVERVIEW OF RELEVANT TECHNOLOGIES

Around-the-corner detection and NLOS radars, which the paper is focusing on, have already been addressed to some extent in the existing literature. For example, in [6] and [7] authors successfully recognized a human, standing in a NLOS tunnel and T-shaped room, by performing 2.5–3.5 GHz and 24 GHz radar measurements. A similar study is reported in [8], where a mobile human being, hidden behind a concrete wall, was identified by radar. In these studies, the illuminating signal that is used for target detection is propagating without employing additional artificial reflectors. Nevertheless, such implementation is topology and scenario dependent and may not work in some other deployments. Specifically, the results in [4] show that NLOS detection is very challenging in practical urban blind intersections, where the signal cannot find a low-loss way to the around-the-corner region. Therefore, an intriguing research prospect is to consider artificial features or added material constructions to assist the NLOS around-the-corner detection.

An alternative approach to the proposed passive reflector considered in this work is to install and consider road-side units (RSU) on the buildings, discussed, e.g. in [9]–[12], to warn the vehicles about the potential collision risk. This solution fits the vision of the 3 rd Generation Partnership Project (3GPP), where all vehicles are eventually going to be connected to the infrastructure (vehicle-to-infrastructure communication, i.e. V2X) network. However, the realization of this idea in dense mobile urban conditions might be challenging due to possible problems with finding a sufficient amount of sites for deploying active RSUs as well as with the resource allocation. Furthermore, this solution is still primarily limited to lab prototypes, while the radars are already commercially available and thoroughly spread and deployed. Finally, following the standardization timeline, it is still likely to take many years before the RSUs may find their way to large scale deployments at the urban crossroads. We also note that the Global Positioning System (GPS) or other relevant satellite-based positioning systems such as Glonass, Galileo, Beidou, etc., can be also taken into consideration for avoiding collisions at intersections. For example, authors in [13] propose to exploit GPS communication specifically for collision avoidance. However, typical urban scenarios may experience significant positioning errors [14], especially in cities with high-rise buildings, which degrade the overall reliability of satellite positioning based methods.

Alternatively to the radio frequency (RF) based solutions, optical systems may also be considered and engaged for the NLOS detection. For example, promising results in [15]–[17] proof the ability to detect objects behind an opaque wall by the joint operation of laser and ultra-fast camera. Such cooperative action has some conceptual similarities to the proposed NLOS radar scheme, where the camera and laser act as receiver and transmitter, respectively. Moreover, some of the literature sources such as [18] offer to embed this idea in the LIDAR functionality. However, the operation of the NLOS laser-based method in harsh outdoor conditions with finely dispersed particles – say fog, rain, dirt, etc. – can easily be challenging. Specifically, the natural limitation of the light associated with scattering and attenuation

effects may crucially reduce the reliability of the laser-based solutions [19]. For the same reasons, the performance of image processing of video cameras [20] can also be clearly limited. On the contrary, due to larger wavelengths even at the mmWave bands compared to the optical frequencies, the proposed RF-based radar scheme is less affected by the harsh environmental conditions compared to the optical solutions.

In general, passive reflecting surfaces play an essential role in radar testing. The most popular of these is the corner reflector, returning the signal precisely to the source point. To this end, smart surfaces are currently being actively studied and considered, for example, in the context of 6 G systems [21], [22]. Recent advances in metamaterials offer the prospect of deploying smart surfaces, or intelligent reflecting surfaces (IRS), that can manipulate EM channels. For example, the so-called programmable channel concepts in the context of multi-user multiple-input and multiple-output (MU-MIMO) transmission and beamforming are studied in [23]. In [24], IRS technologies are emerging as an important paradigm for the realisation of smart radio environments, where large numbers of small, low-cost and passive elements reflect the incident signal with an adjustable phase shift. In [25], the use of passive reflectors for improving signal coverage in NLOS indoor areas is investigated. Importantly, however, it is noted that all these smart surface technologies are associated with relatively high cost while also requiring a power supply. Oppositely, this paper focuses on the deployment of a lower-cost and technologically more simple purely passive reflector solution. While being more likely to allow for large-scale deployments, because of the reduced costs and ability to operate without an active power source, the absence of any structural and functional elements in the construction of the passive reflector may also increase the reliability of the proposed scheme in typical harsh outdoor environments.

## III. DEPLOYMENT SCENARIO AND MEASUREMENT EQUIPMENT

The topology of interest is an urban blind intersection where buildings obstruct the LOS visibility between the two approaching vehicles, driving along the perpendicular roads. The considered example deployment scenario at the Hervanta Campus of Tampere University, Finland, is illustrated in Fig. 1(a) within which the mmWave radar measurements are carried out. The detectable car, Kia Ceed, drives along the road, surrounded by two buildings. The car's speed does not exceed 20 km/h for safety reasons in the university campus area. The walls of the surrounding buildings are covered with corrugated metal sheets, and metal pipes are located next to them. Such surrounding metallic surfaces may potentially contribute to the formation of additional multipath components. This statement will be studied more accurately in Section VI-B. A constructional metallized foam-based insulator is employed forming the 1.2 × 1.8 m planar reflector shown on the right side of Fig. 1(a). It is rigidly fixed to a heavy trolley to enable convenient transportation and reliable spatial orientation. The metallized insulator reflects the signal, emitted from the static mmWave radar setup, located at a certain distance. The measuring radar equipment mimics the on-board automotive radar module installed in the near-bumper
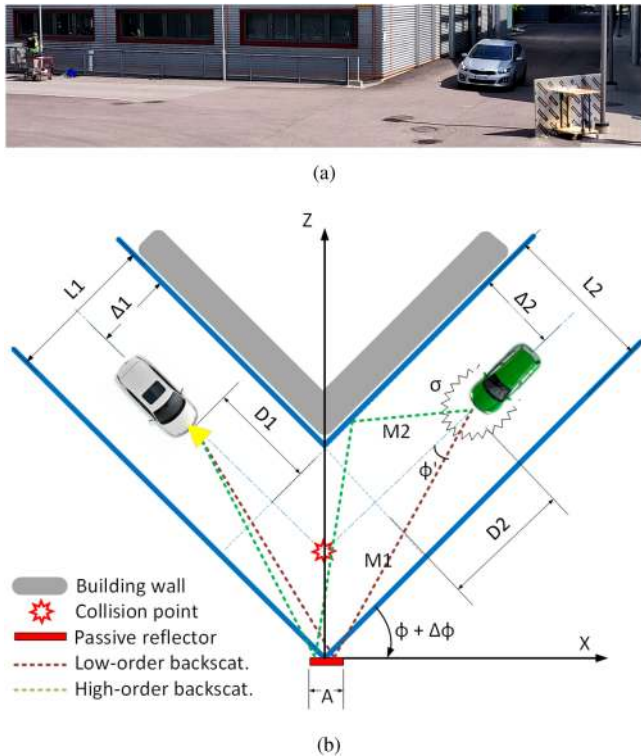
Fig. 1. (a) Photography illustration of the measured deployment scenario with a blind intersection at the Hervanta Campus of Tampere University, Finland. (b) Simplified two-dimensional representation of the deployment scenario for analytical calculations and modeling.

TABLE I
BASIC PARAMETERS OF THE CONSIDERED DEPLOYMENT SCENARIO

| Dimension | Value/Range | Definition |
|---|---|---|
| $L_1$, m | 6.5 | Radar vehicle road width |
| $L_2$, m | 6.5 | Detectable vehicle road width |
| $\Delta_1$, m | 5 | Radar veh. trajectory shift |
| $\Delta_2$, m | 2.25, 3.25, 4.25 | Detect. veh. trajectory shift |
| $D_1$, m | 10 | Static distance of setup |
| $D_2$, m | 50–0 | Driving distance |
| $A$, m | 1.2 x 1.6 | Reflector's area |
| $\phi$, ° | 39.5, 43.5, 47.5 | Reflector's orientation angle |
| $R_r$, m | $\infty$ | Reflector's curvature radius |

zone. The top view simplified representation of the measured deployment scenario, illustrating also the exact dimensions, is shown in Fig. 1(b) and further tabulated in Table I. In general, all the listed parameters match the actual topology. We also note that the angles were chosen experimentally to demonstrate the impact of the reflector's orientation in the most concrete and explicit manner. In particular, after trial measurements, it was determined that a reference angle of 43.5° yields the best performance. To allow for accurate setting of the associated angles, the measurements were carried out with a laser pointer rigidly attached to the reflector.

In this paper, radar measurements are executed by in-house assembled mmWave radar setup, operating at 28 GHz whose detailed description can be found in [26]. The transmitting (TX) and receiving (RX) antennas of this equipment are located at 0.3

m above the ground, which fits the typical height of the radar antenna for vehicle applications [27]. The core part of the measurement setup is a vector signal transceiver (VST), implementing the TX and RX functionalities at an intermediate frequency (IF) of 3.5 GHz. This value perfectly meets the characteristics of filters employed in the setup. Next, two signal generators act as local oscillators to up/down-convert the IF signal to/from the actual carrier frequency of 28 GHz. The modulated orthogonal frequency-division multiplexing (OFDM) signal is fed to horn TX antenna PE9851A-20 from Pasternack with a gain of 20 dBi. The half-power beamwidths (HPBWs) of the antenna, in vertical and horizontals planes, are 17°. The backscattering power is captured by an identical RX horn antenna. In the measurements, OFDM signal with channel bandwidth of 200 MHz and 60 kHz subcarrier spacing is utilized, inline with the 3GPP 5 G New Radio specifications at the mmWave bands [28]. The utilization of an actual data modulated OFDM waveform is deliberately pursued, instead of a dedicated radar waveform, in the spirit of RF convergence [22], [29], [30]. For each of the analyzed deployment configurations listed in Table I, the radar processing and the corresponding radar image construction are carried out 20 times along the route of the vehicle illustrated in Fig. 1. For the radar processing, the subcarrier-domain algorithms, similar to [31], are applied to obtain the backscattering power from all surrounding objects. However, in this paper, only the backscattering power from the driving vehicle is of interest.

## IV. ELECTROMAGNETIC MODELING

### A. Simplified Deployment Model

For the purpose of analytical EM modeling, Fig. 1(b) represents a simplified 2D version of the real-world measured scenario illustrated in Fig. 1(a). The dimensionality reduction from 3D to 2D becomes feasible when the following simplifying assumptions are applied. First, the orientation of the reflector is strictly perpendicular to the road. Second, the reflector shape remains constant along the $y$-axis. Finally, the ground reflected multipath components are neglected, which removes constructive and destructive interference at the RX (for further details, refer to the 2-Ray model and corresponding clarifications in [32]). The last simplification is justified by the inability to accurately consider this phenomenon due to the small wavelength (∼1 cm) and the high complexity stemming from the non-uniform profile and roughness of the road pavement.

Similarly to the measurements, the simplified modelling deployment represents an intersection, where the LOS visibility is obstructed by a building, depicted by the thick grey lines in Fig. 1(b). The detectable (green) and the radar (white) vehicles travel along the perpendicular roads with a potential to collide at the point highlighted with the red star. The driving trajectories (blue dash-dot lines) are shifted by $\Delta_1$ and $\Delta_2$ relative to the blocking building walls. The parameters $L_1$ and $L_2$ characterize the widths of the roads, $A$ denotes the horizontal size of the passive reflector, while $\phi$ refers to the rotation angle. Finally, distance $D_1$ is fixed and defines the position of the radar equipment (radar vehicle in practice), while $D_2$ changes along the

whole driving path of the green detectable vehicle. All these parameters are noted and summarized in Table I.

### B. Radar and Backscattering Power Calculations

According to ITU-R recommendations in [27], the radar range equation (RRE) is a typical approach to calculate the backscattering power in the LOS conditions. In case of the proposed NLOS radar scheme, the reflector acts as an ideal lossless mirror only if $D_1$ and $D_2$ are significantly larger (tens of meters) compared to the wavelength. Therefore, if the reflecting point belongs to the reflector's area, the power backscattering at the RX can in principle be described through the RRE as

$$P_{rre} = \frac{P_1 G_1 G_2 \lambda^2 \sigma}{(4\pi)^3 R^4}, \tag{1}$$

where

$$R \approx \sqrt{(D_1 + L_2)^2 + (L_1 - \Delta_1)^2} + \sqrt{(D_2 + L_1)^2 + (L_2 - \Delta_2)^2}. \tag{2}$$

In (1), $\lambda = 1$ cm denotes the wavelength, $G_1$ and $G_2$ are TX and RX antenna gains equal to 20 dBi, $P_1$ is the 10 dBm transmit power, and finally, $\sigma$ is monostatic radar cross-section (RCS) of the detectable vehicle (the green one in Fig. 1(b)). The total distance $R$ is expressed in (2), where dimensions $D_1$, $D_2$, $L_1$, $L_2$, $\Delta_1$, $\Delta_2$ are shown in Fig. 1(b) and parameterized in Table I.

However, the expression in (1) is applicable only when the detectable object is a "point scatterer" [33], i.e., located in the far-field region. In the considered deployment scenario, the distance $R$ may reach 23 m, at which the detectable vehicle is too far from being a point scatterer. Additionally, the value of the range $D_2$ may further substantiate the case, when the reflecting point is out of the reflector area. Accordingly, a more accurate physical model that takes into account all of the above factors should be developed. This is pursued next.

Stemming from above reasoning, two expressions building on the *Kirchhoff theory* [34] are introduced in this article to calculate the backscattering power accurately. Specifically, the backscattering power from the driving vehicle with flat reflector (surface curvature $R_r = \infty$ m) is first expressed as

$$P_{flat} = \frac{P_1 G_1 G_2 z_2^4 \sigma}{(4\pi)^3} \left| \int_{-\frac{A}{2}}^{\frac{A}{2}} \frac{\exp(-ik(R_1 + R_2))}{R_2 \sqrt{R_1 R_2 (R_1 + R_2)}} dx \right|^4. \tag{3}$$

On the other hand, the backscattering power from the detectable vehicle in the radar scheme with curved reflector ($R_c \neq \infty$ m) can be calculated as

$$P_{curv.} = \frac{P_1 G_1 G_2 R_c^4 \sigma}{1024\pi^3} \left| \int_{-\beta_0}^{\beta_0} \left( \frac{\exp(-ik(R_1 + R_2))}{R_2 \sqrt{R_1 R_2 (R_1 + R_2)}} \right) \times \right.$$
$$\times \left( \frac{(x - x_1)\sin\beta + (z - z_1)\cos\beta}{R_1} + \right.$$
$$\left. \left. + \frac{(x - x_2)\sin\beta + (z - z_2)\cos\beta}{R_2} \right) d\beta \right|^4. \tag{4}$$

The parameters $P_1$, $G_1$, $G_2$ and $\sigma$ in equations (3) and (4) have the same meaning as in (1). The radar-reflector distance $R_1$ and the reflector-car distance $R_2$ as well as the locations of the radar $(x_1, z_1)$ and the detectable car $(x_2, z_2)$ can, in turn, be expressed as

$$R_1 = \sqrt{(x - x_1)^2 + (z - z_1)^2}, \tag{5a}$$

$$R_2 = \sqrt{(x - x_2)^2 + (z - z_2)^2}, \tag{5b}$$

$$x_1 = D_1 \cos\phi + (L_1 - \Delta_2)(\cos\phi - \sin\phi), \tag{5c}$$

$$x_2 = -D_2 \sin\phi + (L_2 - \Delta_1)(\cos\phi - \sin\phi), \tag{5d}$$

$$z_1 = D_1 \sin\phi + (L_1 - \Delta_2)(\cos\phi + \sin\phi), \tag{5e}$$

$$z_2 = D_2 \cos\phi + (L_2 - \Delta_1)(\cos\phi + \sin\phi), \tag{5f}$$

where $L_1$, $L_2$, $\Delta_1$, $\Delta_2$, $D_1$ and $D_2$ are listed in Table I, $k$ is the wavenumber magnitude, while $\phi$ refers to the orientation angle illustrated in Fig. 1(b). Finally, the scattering points of the reflector with radius $R_r$ in equation (4) can be calculated as

$$x = R_r \sin\beta, \tag{6a}$$

$$z = R_r \cos\beta - R_r, \tag{6b}$$

$$\beta_0 = \arcsin(A/2R_r). \tag{6c}$$

For readers' convenience, the derivation details related to (3) are presented in Appendix A, while (4) can be derived and obtained in a very similar way. Furthermore, the numerical results provided in Section VI will validate the correctness and accuracy of the derived analytical model, when compared against the basic RRE approach as well as against full EM simulations in HFSS. We also note that an in-house numerical tool, executable in Matlab Runtime environment, is available in [35] for practical engineering calculations in the context of the consider NLOS radar scheme and the associated modeling equations.

Additionally, we also note that the Doppler shift or spread is not included in (3) and (4). This is because with realistic values of the velocity, the Doppler does not essentially affect the backscattering power. In particular, additional calculations and analysis show that even with an example velocity of 15 m/s, the difference is commonly less than 0.1 dB when comparing to the zero-velocity case.

Finally, we note that in (1), (3) and (4) the RCS of the detectable vehicle $\sigma$ is unknown. Theoretically, it can be found or expressed as [33]

$$\sigma = \lim_{r \to \infty} 4\pi r^2 |E^{scat}|^2 / |E^{inc}|^2. \tag{7}$$

The $E^{inc}$ in (7) denotes the amplitude of the incident plane wave, and $E^{scat}$ indicates the scattered field, representing the superposition of all surface currents. In the case of a perfect electrical conductor (PEC), the flowing surface current does not encounter any attenuation. Oppositely, if the surface is resistive, then the surface current weakens proportionally to the surface impedance $\eta$, that reads

$$\eta = \sqrt{\frac{j\omega\mu}{\sigma' + j\omega\epsilon}} \eta_0. \tag{8}$$

In (8), $\omega$ is angular frequency, $\mu$ and $\epsilon$ are relative permeability and permittivity, respectively, $\sigma'$ is conductivity, and finally, $\eta_0 = 120\pi$ is free space impedance. Since the detectable car has both PEC (body) and resistive (radiator grid, bumper) elements, the expression in (8) can be applied in the EM modelling. Additionally, RCS $\sigma$ is also a function of the incidence angle $\phi'$, expressed as

$$\phi' \approx \arctan\left(\frac{L_2 - \Delta_2}{D_2 + L_1}\right). \tag{9}$$

Substituting the numerical values to (9) gives the following range of $\phi' = 2.5\text{–}35.5°$ when considering the different values of the involved variables listed in Table I.

## V. MMWAVE RADAR MEASUREMENTS

Comprehensive measurements of the backscattering power in the scenario shown in Fig. 1(a) are next carried out by the mmWave radar equipment described in Section III. The setup is initially calibrated to Friis law in the free-space conditions, where 9 dB loss is determined. Next, the radar setup is placed at a location, specified by the distances $D_1$ and $\Delta_1$, while the detectable car is initially located at $\max(D_2)$. Then, by the command of the radar equipment operator, the driver of the detectable car starts driving from $\max(D_2)$ to $\min(D_2)$. During this time that the vehicle is moving, multiple samples of the backscattering power in the form of radar images are captured by the radar setup and stored for further processing and visualization. The measurement procedure is repeated three times per scenario, each of which is characterized by the particular combination of $\Delta_2$ and $\phi$ (see Table I). The total number of the unique scenarios being measured is thus nine.

As an example, one captured radar image is shown in Fig. 2(a), where the red spot at $v = 3.5$ m/s corresponds to the backscattering power from the detectable vehicle, located at $D_2 = 16$ m. It can be also observed that there are multiple spots or 'targets' at $v = 0$ m/s, exposing the unwanted backscattering power or clutter from the surrounding *static* environmental objects. Therefore, in order to discard the less useful data or focus on the essential area in the radar image, the rectangular region of interest – outlined by dashed lines in Fig. 2(a) and specified by velocity and distance ranges of $v = 2\text{–}5$ m/s and $D_2 = 3\text{–}50$ m, respectively – is introduced. These values are basically stemming from the overlaid radar observations in Fig. 2(c)-2(e). Then, inside this window of interest, the maximal backscattering power is always detected and stored as a function of $D_2$. It is also noted that such filtering does not perform very well in some scenarios, due to spurious power stemming most likely from some hardware artifacts that are strictly speaking unknown to the authors. This effect is explicitly illustrated in Fig. 2(b), observable at $v = 2$ m/s and $D_2 = 7$ m. Such spurious target, despite being relatively weak, overestimates the power level in the rectangular area in such cases where the actual backscattering power of the detectable vehicle is absent (as in Fig. 2(b)). Accordingly, some additional local windowing is applied to further improve the processed data.
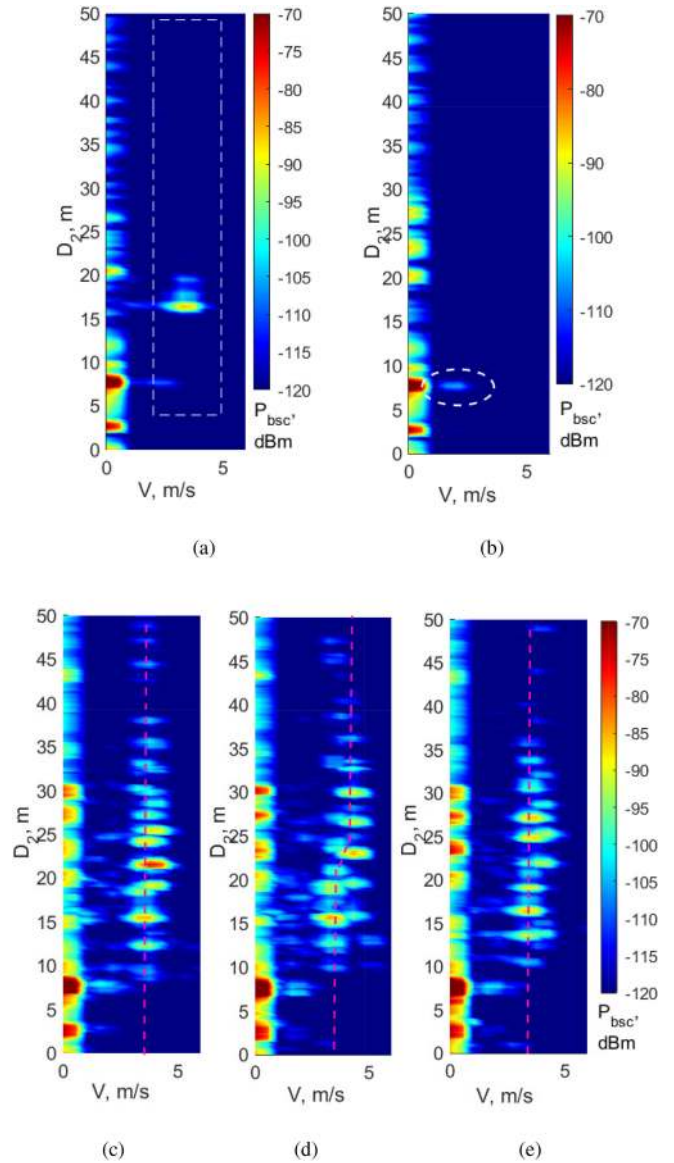


Fig. 2. (a) Radar image snapshot obtained with the mmWave measurements at 28 GHz, where a backscattering power of -86 dBm from the driving vehicle is detected at $D_2 = 16$ m. (b) Another radar image snapshot, with no observable backscattering power from the driving vehicle, but showing spurious low-power target at $D_2 = 7$ m. (c)-(e) Three consecutive measurement attempts of the same scenario with overlaid radar snapshots along the movement of the detectable car.

The backscattering peak, illustrated in Fig. 2(a), moves synchronously with the detectable car from $\max(D_2)$ to $\min(D_2)$. This effect is depicted in Fig. 2(c)–2(e), where multiple radar images are overlaid in the same subfigure. The subfigures c)-e) describe three measurement attempts in the same scenario with $\Delta_2 = 2.25$ m and $\phi = 43.5°$. It can be noticed that despite the same scenario, the three pictures demonstrate slightly different patterns of the backscattering power, stemming at least from the following reasons. Firstly, the human driver cannot repeat exactly the same velocity and acceleration profiles in different measurement attempts. Moreover, the driver is not able to keep the ideally constant dynamics of the car during driving within an attempt. As an example, the red dashed line in Fig. 2(d) shows a
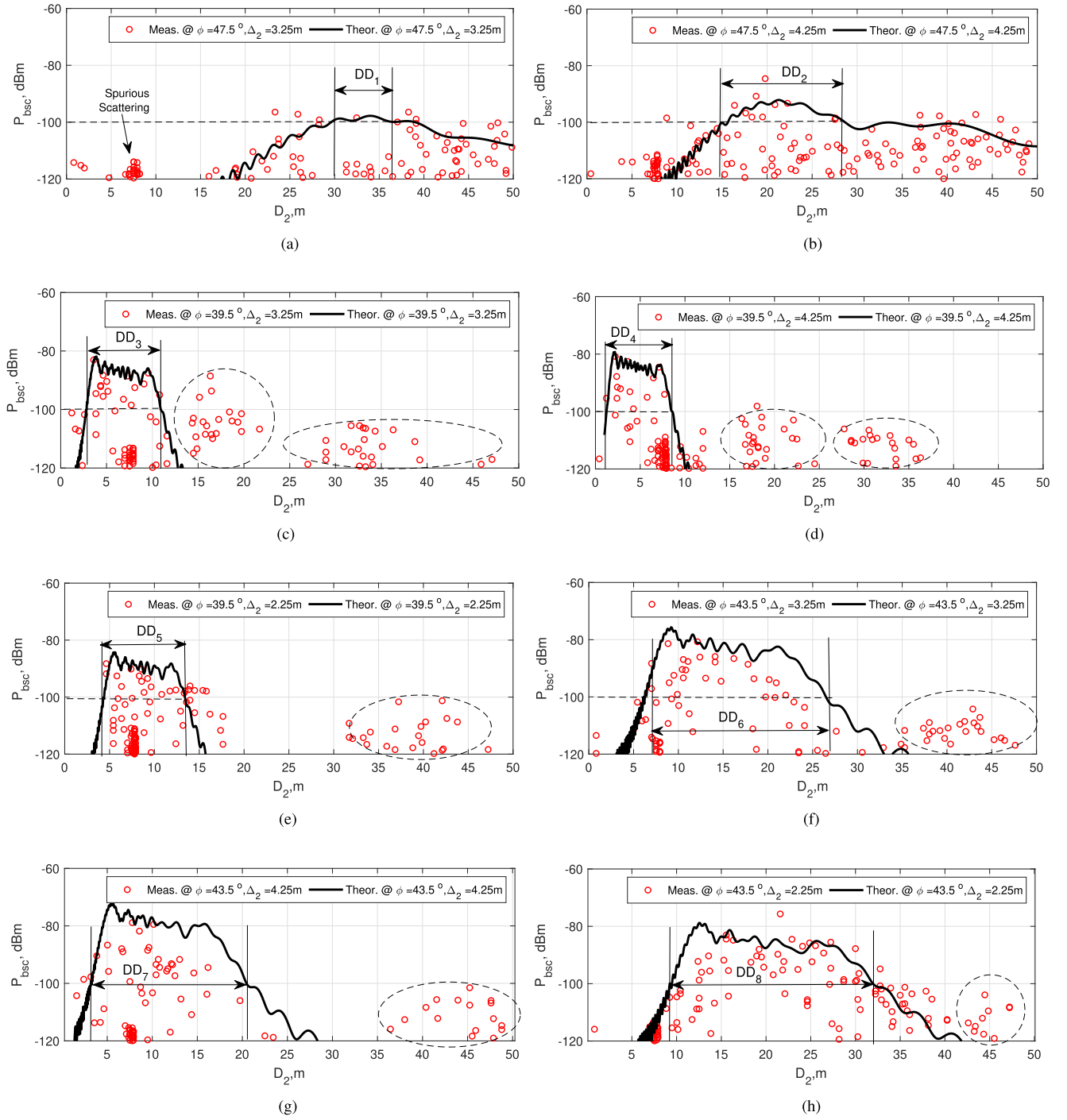
Fig. 3.    Comparison between measured and analytical/simulated backscattering powers as functions of $\Delta_2$ while considering different values of $\phi$. The following constant parameter values were utilized: A = 1.6 m, $L_1$ = 6.5 m, $D_1$ = 10 m, and $\Delta_1$ = 5 m. The value of the RCS $\sigma(\phi')$ varies from -7 dBsm to 10 dBsm according to Fig. 4(b).

velocity change by 0.6 m/s after some 20 m of driving. Secondly, despite the presence of road markers, the position of the car was varying up to roughly 0.20 m. Thirdly, the radar operator is subject to uncertainty in the exact start time of the recording, most likely up to 1 s, which undoubtedly affect the interpretation of the individual measurement traces.

All the measured and stored backscattering powers for different measured scenarios are plotted with red circles in Fig. 3. The analysis of the results and their comparison to analytical models and EM simulations are provided in the next section. The measurement data is openly available in [35] for reproducible research and any potential follow-up work.

TABLE II
MATERIALS UTILIZED FOR SIMULATION IN HFSS

| Part | Material | $\epsilon$ | $\sigma'$, S/m | $\tan\delta$ | $\eta$ | Ref. |
|---|---|---|---|---|---|---|
| Windshield | Glass | 6.4 | 0.1 | 0.011 | 150 | [39] |
| Bumper | Polymer | 2.5 | 0.02 | 0.005 | 238 | [39] |
| Radiator grid | Polymer | 2.5 | 0.02 | 0.005 | 238 | [39] |
| Light beam | Polymer | 2.5 | 0.02 | 0.005 | 238 | [39] |
| Body | PEC | 1 | $10^{30}$ | 0 | 0 | HFSS DB |

## VI. FINAL MODELING RESULTS AND ANALYSIS

### A. EM Simulation of Radar Cross-Section

To supplement the evaluation of the analytical backscattering power expressions, the EM modelling of the RCS $\sigma$ is next executed in Ansys HFSS, where the shooting and bouncing ray (SBR+) method with the uniform theory of diffraction (UTD) and physical optics (PO) are applied [36]. These methods are the most accurate and computationally efficient for electrically large objects compared to the alternative full-wave methods. According to [36], SBR+ supports dielectric materials and boundary conditions, which empowers to assign different materials to the EM car model. Therefore, in this paper, the *impedance boundary condition* is applied to all the dielectric parts, while alternative boundary conditions – called in HFSS as *finite conductivity* – are aimed for good conductors [37]. All material are listed in Table II and highlighted through different colors in Fig. 4(a).

The computer-aided design (CAD) model of Kia Ceed [38] is selected for HFSS simulation due to the list of fulfilled requirements. First, the selected 3D CAD-model is seemingly geometrically precise, that can be also inferred by the file size of 30–50 MB. The rule-of-thumb range, showing a right balance between computational time and the output accuracy, is determined experimentally in [5]. Furthermore, the detailed examination of the model shows sufficient density and good quality of the facets. Specifically, they have the lowest aspect ratio and do not produce sharp stitches. Secondly, the selected 3D CAD-model is an assembly (*.asm) of separate solid parts (ring disks, glass parts, headlights), to which materials in Table II can be assigned. The values for dielectric permittivity $\epsilon$, conductivity $\sigma$, and loss tangent $\tan\delta$ are taken from the HFSS database and from [39], while impedance $\eta$ is calculated with the expression in (8).

To shorten the computational time in HFSS, some preprocessing of the 3D model is also utilized. First, the surfaces or elements committing very low-level backscattering power are removed. Such surfaces or elements are primarily characterized by their small size, high surface impedance $\eta$, and/or orientation of their normals perpendicular to the wave vector of incident signal (roof, for instance) [5]. Additionally, interior elements and rear parts of the car are removed (see Fig. 4(a)), due to inability to model signal penetration into an object in HFSS. Despite such simplifications, the calculation time on the high-performance Lenovo Thinkpad P53 took more than 20 hours.

The simulation of the monostatic $\sigma$ is performed in the frequency range of 27.5–28.5 GHz with 0.1 GHz step, while the plane wave sources/receivers are distributed around the front part of the 3D model within the range of $\phi'$ varying from -40.0°
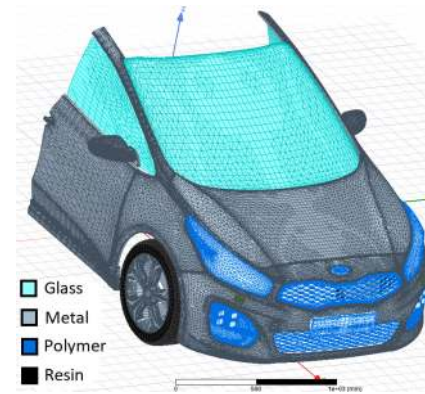


(a)
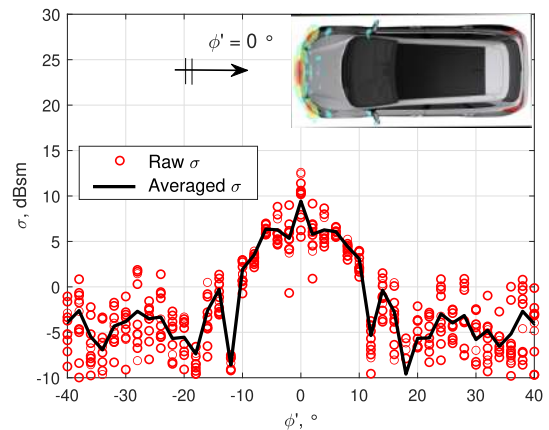


(b)

Fig. 4. (a) Illustration of the utilized 3D model of Kia Ceed with assigned materials. (b) Multi-frequency raw (red circles) and averaged (black) RCS values ($\sigma$) of Kia Ceed simulated in Ansys HFSS.

to 40.0° with respect to longitudinal central axis. The direction of incidence at $\phi' = 0°$ is strictly perpendicular to the license plate and coincides with the longitudinal axis. The results of the simulated RCS $\sigma$ are shown in Fig. 4(b). Because of the high variations of the simulated data (red circles), a smoothing filter representing averaging over the frequency range of 27.5–28.5 GHz with 0.1 GHz step is next applied, yielding the smooth black dashed curve shown in the figure. It can be seen that the maximum 10 dBsm scattering gain occurs from the front bumper at $\phi' = 0°$, and decreases to -7 dBsm already at $\phi' = 12°$. Based on (9), the angle $\phi'$ varies from 2.5° to 35.5° which corresponds to $\sigma$ range from 10 dBsm down to -7 dBsm. This obtained distribution or range for the RCS $\sigma$ will be substituted in expressions (3) and (4) in order to evaluate the backscattering power characteristics, while then also comparing to the corresponding measurement based results. These are pursued next.

### B. Assessment of the Backscattering Power

Next, the derived expressions in (3) and (4) are employed to calculate the analytical backscattering power while comparing

with the actual measured data from the mmWave radar experiments. The input data is taken from the Table I. The analytical results are shown as solid black lines in Fig. 3. It can be observed that the analytical results predict well only certain parts of the measured data. Oppositely, other groups of measured samples, outlined with dashed ellipses, are also observed in the measured data that are not directly disclosed by the analytical expressions.

In order to explain the observed phenomenon, let us next decompose the entire data into two subsets. One of them is the *low-order backscattering*, where radiated and returned radar signal interacts only with the reflector and the detectable vehicle (brown dashed line $M_1$ in Fig. 1(b)). This paper focuses in particular on this phenomenon, while the expressions in (3) and (4) seek to describe it analytically. In Fig. 3(c)–3(h), the low-order backscattering flat-topped pulse appears closer to $\min(D_2)$ than the data in ellipses, due to the shortest propagation path. If the orientation angle $\phi$ reduces (counterclockwise rotation), the registered low-order backscattering pulse moves to the shorter $D_2$ (compare Fig. 3(c) and 3(e)). Oppositely, if $\phi$ increases (clockwise rotation), then the reflector scatters the signal almost along the road, which enables the detection of the approaching vehicle at far distances meaning larger values of $D_2$. In Fig. 3(a)–3(b), the backscattering flat-top pulse embeds into the distribution, with the low-order part becoming essentially non-distinguishable.

Stemming from the results, the angle value of $\phi = 43.5°$ is identified as optimal in the selected scenario and geometry for the two reasons. First, the received backscattering power at $\phi = 43.5°$ is higher than at $\phi = 39.5°$ and comparable with $\phi = 47.5°$, which guarantees receiving the radar signal above the noise floor. Another important criterion is the *detection distance* denoted as $DD$ in Fig. 3. Specifically, larger $DD$ provides more time to the radar vehicle to collect statistics about the approaching car. For example, if the car speed is 20 m/s and the radar image sampling rate of the radar system is 0.1 s, then 10 samples with $P_{bsc} \geq$ -100 dBm can be captured at $DD_6 = 20$ m in Fig. 3(f) while already less than 5 samples at $DD_5 = 10$ m in Fig. 3(e). Alternatively, the longest $DD$ might be considered in Fig. 3(a) or 3(b) for $P_{bsc} \leq$ -100 dBm. However, the power levels close to the noise floor can be impractical. Therefore, results for the radar scheme where the reflector is oriented at $\phi = 43.5°$ can be considered most reliable and representative for the selected deployment scenario.

Another subset of the obtained data is the *high-order backscattering* (measured data in dashed ellipses in Fig. 3), where the radiated and returned radar signal interacts with the detectable car, reflector, and the building wall elements (green dashed line in Fig. 1(b)) and the additional metallic parts. This data subset appears after the low-order backscattering as a cluster (Fig. 3(d)) or tail (Fig. 3(h)). Due to the complexity of the measured scenario, the classification, sorting and analytical investigation of such high-order backscattering effects seems highly challenging and requires more precise geometrical measurements and advanced ray tracing simulations.

It should also be noted that in real-life scenarios, the surrounding elements may create and obstruct the irradiated and scattered signal. For example, the transmitted and received signals can
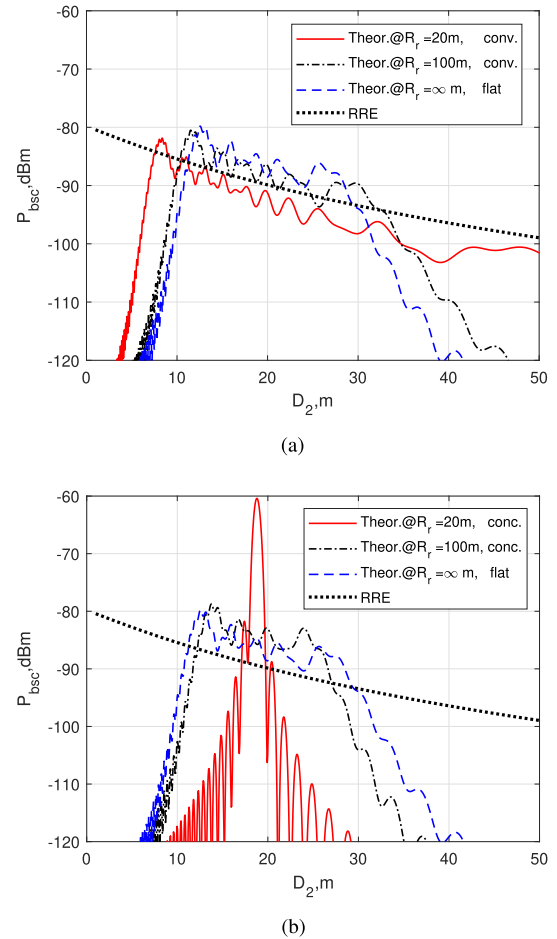


Fig. 5. Analytical calculation results of the backscattering power with (a) convexly curved reflector, and (b) concavely curved reflector.

be blocked by people, vehicles, road infrastructure elements, or trees on the sidewalk. Therefore, the proposed radar scheme may have challenges to operate well in conditions such as a wide avenue with heavy traffic, where the blockage probability is high. Moreover, it is noted that the utilization of the reflector reduces the capabilities to pursue MIMO radar operation, stemming essentially from the keyhole effect [40]. Specifically, because of the low spatial diversity of the multipath components (dominant paths have the same geometry), formed by canyon-like scenario and reflector acting as a "pinhole," the spatial degrees of freedom are reduced. Further analysis and developing potential means to address these limitations form important topics for our future work and research.

Lastly, we pursue an analytical investigation of the curved reflector through the expression in (4), whose scattering capabilities are also preliminarily studied in [5]. In particular, the EM modelling results showed that a convexly curved surface exhibits a wider angular dispersion of the scattered field compared to a flat surface. As a result, it may potentially increase the width $DD$ in Fig 3. The corresponding results of the backscattering power in the proposed radar scheme with curved and flat reflectors, respectively, are demonstrated in Fig. 5(a). Specifically, in this

figure, three different radiuses $R_r$ of a convexly curved surface are compared to the flat reflector. Both these shapes have similar area $A$ listed in Table I. It can be seen that the smallest radius of 20 m (the solid red line in Fig. 5(a)) prevents sharp decreasing of the backscattering flat-top pulse and increases the $DD$ as expected. Oppositely, the maximal power level at $R_r = 20$ m slightly drops relative to the RRE (black dotted line). At the same time, in case of $R_r = 100$ m, the shape of the backscattering pulse becomes comparable to a flat reflector (dashed blue line), having basically infinitely large $R_r$. Alternatively, if the shape is concave (see Fig. 5(b)), then $DD$ reduces, and the observation becomes more focused in the distance domain. The latter fact can be seen as a narrow peak (the solid red line) of the backscattering power, which is some 20 dB higher than the corresponding RRE based curve. Based on Fig. 5(a) and 5(b), the convex reflector with 20 m curvature radius looks preferable for the practical applications in the considered scenario type of deployments.

## VII. CONCLUSION

In this article, a radar scheme aided with a passive reflector was studied and investigated, in order to allow for non-line-of-sight vehicle detection and thereon to reduce the collision probability in blind intersections. In the considered scheme, the signal transmitted by the automotive radar propagates to the detectable vehicle and back while interacting with the passive reflector. Therefore, the observable backscattering power at the radar receiver is selected as the main metric of interest to investigate the performance of the NLOS radar scheme. First, practical mmWave measurements were carried out at 28 GHz, considering an example vehicular deployment scenario at the Hervanta Campus of Tampere University, Finland, with in-house radar equipment. Then, analytical expressions were derived and provided, stemming from the Kirchhoff theory, to character-ize and calculate the backscattering power while calibrating the model with the measurement based results. The obtained analytical curves fit the shape and position of the measured data while providing also some additional information. For example, visualizing, analyzing and comparing the analytical and measured data discovered two clusters of the received backscattering power created by propagation paths interact-ing and non-interacting with the building walls and metallic elements.

Additionally, in the considered deployment scenario context, the optimal orientation angle of the reflector was determined by the power level and duration of the low-order backscattering pulse. Specifically, the probability of detecting the around-corner vehicle rises proportionally to the received power level and the duration of the low-order backscattering pulse. Stem-ming from this, an orientation angle of $\phi = 43.5°$ was determined as the most appropriate one in the considered deployment sce-nario. Finally, the convexly/concavely curved and flat reflectors were also investigated analytically. As a result, it was found that convex reflector with 20 m curvature radius produces a wider pulse of the backscattering power. Therefore, the utilization of reflectors with such shape can be considered a promising approach, preferable to a flat reflector. Our future work will focus on extending the modeling and analysis of the NLOS radar scheme to MIMO radar context, consisting of, e.g., the deployment of passive and active surfaces while also addressing the potential limits in the spatial degrees of freedom and their impact on the radar performance.

## APPENDIX A
### DERIVATION OF (3) FOR FLAT REFLECTOR

General expression for the electrical field $E$ from the TX point source at a distance $R$ can first be written as

$$E = \sqrt{\frac{P_1 G_1 \eta_0}{4\pi}} \frac{\exp(-ikR)}{R} = D \frac{\exp(-ikR)}{R}, \quad (10)$$

where $\eta_0 = 120\pi$ Ohm is the free space impedance, $P_1$ is the transmit power, $G_1$ is the transmit antenna gain, and $k$ is the magnitude of the wavenumber. Based on this, let us first find the field $E_2$, impinging on the detectable vehicle with RCS $\sigma$, after being redirected by the reflector. Let us assume that $E_2$ can be expressed in the form of $E_2 = D \cdot S(\rho_1, \rho_2)$, where $S$ is an unknown coefficient. Then, the power flow density can be written as $\overline{p_2} = |E_2|^2/\eta_0$, and thereon the power flux scattered by the car at a distance $R$ reads $\overline{p_3} = \overline{p_2}\sigma/4\pi R^2$. Therefore, $E_3$ is created by a point source and can be described as $|E_3| = \sqrt{\overline{p_3}\eta_0}$. This expression can be rewritten with an introduced phase as follows

$$E_3 = \sqrt{\frac{\overline{p_2}\sigma\eta_0}{4\pi}} \frac{\exp(-ikR)}{R} = |E_2|\sqrt{\frac{\sigma}{4\pi}} \frac{\exp(-ikR)}{R} =$$
$$= D|S(\rho_1, \rho_2)|\sqrt{\frac{\sigma}{4\pi}} \frac{\exp(-ikR)}{R} = F\frac{\exp(-ikR)}{R}, \quad (11)$$

where

$$F = D|S(\rho_1, \rho_2)|\sqrt{\frac{\sigma}{4\pi}}. \quad (12)$$

Next, we apply the principle of reciprocity. If the source $D\frac{\exp(-ikR)}{R}$ at any abstract point 1 creates a field at any other ab-stract point 2 such that $|E_2| = D|S|$, then the source $F\frac{\exp(-ikR)}{R}$ placed at the point 2 gives the field at the point 1 that can be expressed

$$E_{rx} = F|S| = D|S|^2 \frac{\sigma}{4\pi} = \sqrt{P_1 G_1 \sigma \eta_0} \frac{|S|^2}{4\pi}. \quad (13)$$

Therefore, the power flow near the RX antenna reads

$$\overline{p_{rx}} = \frac{P_1 G_1 \sigma}{(4\pi)^2} |S|^4, \quad (14)$$

while the backscattering power can be calculated as

$$P_2 = \frac{P_1 G_1 G_2 \sigma \lambda^2}{(4\pi)^3} |S|^4. \quad (15)$$

Accordingly, the general problem for any type of reflector is to find $S(\rho_1, \rho_2)$ in (15). Below the problem is solved for the case of flat reflector.

Let us reuse the points 1 and 2 in our application context. To this end, let us assume that the radar vehicle is located at the point 1 characterized by $(x_1, y_1, z_1)$, and $r_1$ is the

distance from point 1 to point $(x, y, z)$ on the reflector's surface. Then, $r_2$ is the distance from the reflector to the point 2, located in position $(x_2, y_2, z_2)$. Then, the distances $r_1$ and $r_2$ can be written as $r_1 = \sqrt{(x - x_1)^2 + (z - z_1)^2 + y^2}$ and $r_2 = \sqrt{(x - x_2)^2 + (z - z_2)^2 + y^2}$. The $E_2(x_2, z_2)$ can be calculated if the field, being re-reflected by the surface, at the point $(x, y, z)$ is known. The calculation of this can be completed by the Kirchhoff formula (simplified, the Rayleigh version, valid for flat objects), that states

$$E_2(x_2, z_2) = \frac{1}{2\pi} \int_S E_2(x, y, z) \frac{\partial \psi(r_2)}{\partial \vec{n}} dS, \quad (16)$$

where $\psi(r_2) = \frac{exp(-ikr_2)}{r_2}$ while $\vec{n}$ refers to the unit vector normal to the surface. Integration is performed over the reflector's surface $S$. The derivative along the normal of the function $\psi$ can be calculated as $\partial\psi/\partial\vec{n} = grad(\psi \cdot \vec{n})$. Accordingly, a straightforward question of what $E_2$ is on the surface $S$ arises. Based on the boundary conditions, the tangential component of the total electric field on the metal is zero, i.e. $D\frac{exp(-ikR)}{R} + E_2(x, y, z) = 0$. Thus, the reflection coefficient $\Gamma = -1$. Therefore, $E_2$ should be negative. Additionally, the following important issue is to be noted. Integration in (16) is carried out only over the reflector surface $S$. However, the perturbed field on the edges, contributing to the formation of the scattered signal, is not considered. Therefore, the expression in (16) should be considered only as an approximation. Nevertheless, the Kirchhoff approximation gives a small error for diffraction problems on large objects (large when compared to the wavelength), and mainly in the directions coinciding with the directions of the mirror plane (especially in the shadow region).

The next step is to calculate $S(\rho 1, \rho 2)$ for the considered flat reflector. Incident field $D\frac{exp(-ik)\sqrt{(x-x_1)^2+(z-z_1)^2+y^2}}{\sqrt{(x-x_1)^2+(z-z_1)^2+y^2}}$ taken with a minus sign can be expressed as

$$E_2 = -D\frac{\exp(-ik)\sqrt{(x - x_1)^2 + (z - z_1)^2 + y^2}}{\sqrt{(x - x_1)^2 + (z - z_1)^2 + y^2}}. \quad (17)$$

Next, let us take the derivative of the function $\psi$, written as

$$\frac{\partial\psi}{\partial n} = \frac{\partial\psi}{\partial z} = -\left(ik + \frac{1}{r_2}\right)\left(\frac{\exp(-ikr_2)}{r_2}\right)\left(\frac{z - z_2}{r_2}\right), \quad (18)$$

which for the metallic surface and $kr_2 \gg 1$ can be rewritten as

$$\frac{\partial\psi}{\partial n}(z = 0) = \frac{ikz_2 \exp(-ik\sqrt{(x - x_2)^2 + z_2^2 + y^2})}{(x - x_2)^2 + z_2^2 + y^2}. \quad (19)$$

Finally, the expression for $E_2$ has the following form

$$E_2(x_2, z_2)$$
$$= -\frac{ikz_2 D}{2\pi} \int_S \frac{\exp(-ik(\sqrt{R_1^2 + y^2} + \sqrt{R_2^2 + y^2}))}{\sqrt{R_1^2 + y^2}(R_2^2 + y^2)} dS, \quad (20)$$

where the $R_1$ and $R_2$ are as given in (5 a) and (5 b). This integral over the mirror surface is calculated from $-A/2$ to $+A/2$ on the $x$-axis, and within the corresponding vertical dimensions on

the $y$-axis. For given distances and the wavelength in Table II, the signal does not propagate beyond the vertical reflector's region. Therefore, the stationary phase approximation method is employed to calculate the integral over $y$, where the finite limits of integration are replaced by infinite ones, yielding

$$I = \int_{-\infty}^{\infty} h(y)e^{-ik\phi(y)}dy = \sqrt{\frac{-i2\pi}{k\phi(y_s)}}h(y_s)\exp(-ik\phi(y_s'')), \quad (21)$$

where the stationary point $(y_s)$ is found through $\phi'(y) = 0$. Specifically, in our case,

$$h(y) = -\frac{ikz_2 D}{2\pi(R_2^2 + y^2)\}\sqrt{R_1^2 + y^2}}, \quad (22a)$$

$$\phi(y) = \sqrt{R_1^2 + y^2} + \sqrt{R_2^2 + y^2}, \quad (22b)$$

$$\phi'(y) = \frac{y}{\sqrt{R_1^2 + y^2}} + \frac{y}{\sqrt{R_2^2 + y^2}}, \quad (22c)$$

$$\phi''(y) = \frac{R_1^2}{(R_1^2 + y^2)^{\frac{3}{2}}} + \frac{R_2^2}{(R_2^2 + y^2)^{\frac{3}{2}}}. \quad (22d)$$

Therefore, $y_s = 0$. Then $h(y_s)$, $\phi(y_s)$, and $\phi''(y_s)$ can be expressed as

$$h(y_s) = -\frac{ikz_2 D}{2\pi R_1 R_2^2}, \quad (23a)$$

$$\phi(y_s) = R_1 + R_2, \quad (23b)$$

$$\phi''(y_s) = \frac{R_1 + R_2}{R_1 R_2}. \quad (23c)$$

Substitution of these expressions into (21) yields the following equation of the form

$$E_2 = \frac{\exp(i\frac{\pi}{4})\sqrt{k}z_2 D}{\sqrt{2\pi}} \int_{-\frac{A}{2}}^{\frac{A}{2}} \frac{\exp(-ik(R_1 + R_2))}{R_2\sqrt{R_1 R_2(R_1 + R_2)}}dx, \quad (24)$$

where

$$\left|S(\rho_1, \rho_2)\right|^4 = \frac{z_2^4}{\lambda^2}\left|\int_{-\frac{A}{2}}^{\frac{A}{2}} \frac{\exp(-ik(R_1 + R_2))}{R_2\sqrt{R_1 R_2(R_1 + R_2)}}dx\right|^4. \quad (25)$$

Finally, substitution of (25) in (15) provides the final expression of the backscattering power in the scheme with passive flat reflector noted in (3).

### REFERENCES

[1] K. Mays, "Which cars have self-driving features for 2019?" May 2019. Accessed: Jul. 7, 2021. [Online]. Available: https://www.cars.com/articles/which-cars-have-self-driving-features-for-2019-402645/

[2] V. K. Kukkala, J. Tunnell, S. Pasricha, and T. Bradley, "Advanced driver-assistance systems: A path toward autonomous vehicles," *IEEE Consum. Electron. Mag.*, vol. 7, no. 5, pp. 18–25, Sep. 2018.

[3] H. Wu, F. Qi, J. Wang, and Y. Wang, "Millimeter-wave radar image analysis for the traffic sensing," *J. Phys.: Conf. Ser.*, vol. 1507, no. 5, 2020, Art. no. 052014.

[4] D. Solomitckii, C. B. Barneto, M. Turunen, M. Allén, Y. Koucheryavy, and M. Valkama, "Millimeter-wave automotive radar scheme with passive reflector for blind corner conditions," in *Proc. 14th Eur. Conf. Antennas Propag.*, 2020, pp. 1–5.

[5] D. Solomitckii, M. Heino, S. Buddappagari, M. A. Hein, and M. Valkama, "Radar scheme with raised reflector for NLOS vehicle detection," *IEEE Trans. Intell. Transp. Syst.*, Jun. 2021.

[6] O. Rabaste, E. Colin-Koeniguer, D. Poullin, A. Cheraly, J.-F. Pétex, and H.-K. Phan, "Around-the-corner radar: Detection of a human being in non-line of sight," *IET Radar, Sonar Navigation*, vol. 9, no. 6, pp. 660–668, Jun. 2015.

[7] T. Khac-Phuc-Hung *et al.*, "Around-the-corner radar: Detection and localization of a target in non-line of sight," in *Proc. IEEE Radar Conf.*, Jun. 2017, pp. 0 842–0847.

[8] A. Sume *et al.*, "Radar detection of moving targets behind corners," *IEEE Trans. Geosci. Remote Sens.*, vol. 49, no. 6, pp. 2259–2267, Jan. 2011.

[9] J. Wu, M. Fang, H. Li, and X. Li, "RSU-assisted traffic-aware routing based on reinforcement learning for urban vanets," *IEEE Access*, vol. 8, pp. 5733–5748, 2020.

[10] A. Ali, N. González-Prelcic, and A. Ghosh, "Passive radar at the roadside unit to configure millimeter wave vehicle-to-infrastructure links," *IEEE Trans. Veh. Technol.*, vol. 69, no. 12, pp. 14 903–14 917, Dec. 2020.

[11] J. A. del Peral-Rosado, G. Seco-Granados, S. Kim, and J. A. López-Salcedo, "Network design for accurate vehicle localization," *IEEE Trans. Veh. Technol.*, vol. 68, no. 5, pp. 4316–4327, May 2019.

[12] L. Xue, Y. Yang, and D. Dong, "Roadside infrastructure planning scheme for the urban vehicular networks," *Transp. Res. Procedia*, vol. 25, pp. 1380–1396, 2017.

[13] J. Ahrens, "Development of V2V and GPS based collision warning algorithm for uncontrolled intersections," in *Proc. Electron.*, 2017, pp. 1–4.

[14] A. Angrisano, C. Gioia, S. Gaglione, and G. Del Core, "GNSS reliability testing in signal-degraded scenario," *Int. J. Navigation Observ.*, vol. 2013, 2013.

[15] V. Arellano, D. Gutierrez, and A. Jarabo, "Fast back-projection for non-line of sight reconstruction," *Opt. Exp.*, vol. 25, no. 10, pp. 11 574–11 583, May 2017.

[16] G. Musarra *et al.*, "Non-line-of-sight three-dimensional imaging with a single-pixel camera," *Phys. Rev. Appl.*, vol. 12, no. 1, Jul. 2019, Art. no. 011002.

[17] X. Liu *et al.*, "Non-line-of-sight imaging using phasor-field virtual wave optics," *Nature*, vol. 572, no. 7771, pp. 620–623, Aug. 2019.

[18] A. Kirmani, T. Hutchison, J. Davis, and R. Raskar, "Looking around the corner using transient imaging," in *Proc. IEEE 12th Int. Conf. Comput. Vis.*, Jul. 2009, pp. 159–166.

[19] P. F. McManamon, *LiDAR Technologies and Systems*. Bellingham, WA, USA: SPIE Press, 2019.

[20] J. Guerrero-Ibáñez, S. Zeadally, and J. Contreras-Castillo, "Sensor technologies for intelligent transportation systems," *Sensors*, vol. 18, no. 4, 2018, Art. no. 1212.

[21] Z. Zhang *et al.*, "6 g wireless networks: Vision, requirements, architecture, and key technologies," *IEEE Veh. Technol. Mag.*, vol. 14, no. 3, pp. 28–41, Sep. 2019.

[22] C. De Lima *et al.*, "Convergent communication, sensing and localization in 6 G systems: An overview of technologies, opportunities and challenges," *IEEE Access*, vol. 9, pp. 26 902–26 925, 2021.

[23] Y. Liu, L. Zhang, B. Yang, W. Guo, and M. A. Imran, "Programmable wireless channel for multi-user MIMO transmission using meta-surface," in *Proc. IEEE Glob. Commun. Conf.*, 2019, pp. 1–6.

[24] A. U. Makarfi, K. M. Rabie, O. Kaiwartya, X. Li, and R. Kharel, "Physical layer security in vehicular networks with reconfigurable intelligent surfaces," in *Proc. IEEE 91st Veh. Technol. Conf.*, 2020, pp. 1–6.

[25] W. Khawaja, O. Ozdemir, Y. Yapici, I. Guvenc, and Y. Kakishima, "Coverage enhancement for mmWave communications using passive reflectors," in *Proc. 11th Glob. Symp. Millimeter Waves*, 2018, pp. 1–6.

[26] C. B. Barneto *et al.*, "High-accuracy radio sensing in 5 G new radio networks: Prospects and self-interference challenge," in *Proc. 53rd Asilomar Conf. Signals, Syst., Comput.*, 2019, pp. 1159–1163.

[27] ITU, "Systems characteristics of automotive radars operating in the frequency band 76-81 GHz for intelligent transport systems applications," Rec. ITU-R M.2057–1, Jan. 2018.

[28] 3GPP, "NR; user equipment (UE) radio transmission and reception; part 2: Range 2 standalone," 3GPP Tech. Spec. TS 38.101-2 V17.0.0, Dec. 2020.

[29] P. Kumari, J. Choi, N. González-Prelcic, and R. W. Heath, "IEEE 802.11ad-based radar: An approach to joint vehicular communication-radar system," *IEEE Trans. Veh. Technol.*, vol. 67, no. 4, pp. 3012–3027, Apr. 2018.

[30] Y. Zeng, Y. Ma, and S. Sun, "Joint radar-communication with cyclic prefixed single carrier waveforms," *IEEE Trans. Veh. Technol.*, vol. 69, no. 4, pp. 4069–4079, Apr. 2020.

[31] M. Braun, "OFDM radar algorithms in mobile communication networks," Ph.D. dissertation, Karlsruhe Inst. Technol., Karlsruhe, Jan. 2014.

[32] E. Zöchmann, K. Guan, and M. Rupp, "Two-ray models in mmwave communications," in *Proc. IEEE 18th Int. Workshop Signal Process. Adv. Wireless Commun.*, 2017, pp. 1–5.

[33] E. F. Knott, J. F. Schaeffer, and M. T. Tulley, *Radar Cross Section*. USA: SciTech Publishing, 2004.

[34] V. Borovikov and B. Kinber, *Geometrical Theory of Diffraction*. London, U.K.: Institution Elect. Eng., 1994.

[35] D. Solomitckii *et al.*, "Dataset and EM tool for the paper entitled millimeter-wave radar scheme with passivereflector for uncontrolled blind urban intersection," Zenodo, 2021. [Online]. Available: https://doi.org/10.5281/zenodo.4698906

[36] M. Commens, "Simulating radar signatures of electrically large targets in ansys HFSS," Mar. 2018. Accessed: Dec. 20, 2020. [Online]. Available: https://www.ansys.com/blog/simulating-radar-signatures-large-targets-ansys-hfss

[37] Ansoft, "An introduction to HFSS fundamental principles, concepts, and use," Canonsburg, PA, USA: Ansoft, 2009.

[38] Cgtrader, "Kia Ceed SW GT-Line 2017 VRAY 3D model," Feb. 2019, Accessed: Jul. 7, 2021. [Online]. Available: https://www.cgtrader.com/3d-models/car/standard/kia-ceed-sw-gt-line-2017-vray

[39] S. S. Zhekov, O. Franek, and G. F. Pedersen, "Dielectric properties of common building materials for ultrawideband propagation studies [*measurements corner*]," *IEEE Antennas Propag. Mag.*, vol. 62, no. 1, pp. 72–81, Feb. 2020.

[40] P. Almers, F. Tufvesson, and A. F. Molisch, "Keyhole effect in MIMO wireless channels: Measurements and theory," *IEEE Trans. Wireless Commun.*, vol. 5, no. 12, pp. 3596–3604, Dec. 2006.

**Dmitrii Solomitckii** received the B.Sc. and M.Sc. degrees in electronics and microelectronics from Saint Petersburg Electrotechnical University "LETI", Saint Petersburg, Russia, in 2006 and 2008, respectively. He is currently a Postdoctoral Research Fellow with the Unit of Electrical Engineering, Tampere University, Tampere, Finland. His research interests include antennas, wave propagation, and PHY signal processing in wireless communication and sensing. He also has a broad practical experience in designing of analogue, digital and mixed electronics for critical applications.

**Carlos Baquero Barneto** received the B.Sc. and M.Sc. degrees in telecommunication engineering from Universidad Politécnica de Madrid, Madrid, Spain, in 2017 and 2018, respectively. He is currently working toward the Doctoral degree with the Unit of Electrical Engineering, Tampere University, Tampere, Finland. His research interest include joint communication and sensing systems design, with particular emphasis on 5G and beyond mobile radio networks.

**Matias Turunen** is currently working toward the M.Sc. degree in electrical engineering with Tampere University, Tampere, Finland. He is also a Research Assistant with the Department of Electrical Engineering, Tampere University. His research interests include inband full-duplex radios with an emphasis on analog RF cancellation, OFDM radar, and 5G new radio systems.

**Markus Allén** received the B.Sc., M.Sc., and D.Sc. degrees in communications engineering from the Tampere University of Technology, Tampere, Finland, in 2008, 2010, and 2015, respectively. He is currently with the Department of Electrical Engineering, Tampere University, as a University Instructor. His current research interests include software-defined radios, 5G-related RF measurements and digital signal processing for radio transceiver linearization.

**George P. Zhabko** was born in Leningrad, Russia, in 1949. He Graduated with a degree in radiophysics and electronics from Leningrad Polytechnic Institute (currently Peter the Great St. Petersburg Polytechnic University (SPbPU)), Saint Petersburg, Russia, in 1972. He is currently a Senior Lecturer with the Higher School of Applied Physics and Space Technologies, SPbPU. His research interests include electromagnetic wave propagation, antennas.

**Sergey V. Zavjalov** was born in Leningrad, Russia, in 1988. He received the B.S., M.S., and Ph.D. degrees in communication systems engineering from the Peter the Great St.Petersburg Polytechnic University (SPbPU), Saint Petersburg, Russia, in 2009, 2011, and 2015, respectively. He is currently an Associate Professor with the Higher School of Applied Physics and Space Technologies, SPbPU. His research interests include digital communications, spectrally efficient signaling, UWB signals, and WiFi.

**Sergey V. Volvenko** was born in Temirtau, Kazakhstan, in 1971. He Graduated with a degree in Radiophysics and Electronics from Tomsk State University, Tomsk, Russia, in 1995. He is currently a Senior Researcher with the Higher School of Applied Physics and Space Technologies of Peter the Great St. Petersburg Polytechnic University, Saint Petersburg, Russia. His current research interests include signal processing, optimal signals for wireless communications, meteor-burst and UWB communication networks, Industrial Internet of Things.

**Mikko Valkama** received the M.Sc. and D.Sc. degrees (both with honors) from the Tampere University of Technology, Tampere, Finland, in 2000 and 2001, respectively. He is currently a Full Professor and the Head of the Unit of Electrical Engineering, Tampere University. His research interests include radio communications, radio localization, and radio-based sensing, with particular emphasis on 5G and beyond mobile radio networks.